Full Paper
doi.org/10.1002/chem.202100817

Crystal Structures of $AlCr_2$ and $MoSi_2$: Same Structure Type vs. Different Bonding Pattern

Milica D. Milosavljević,[a] Ulrich Burkhardt,[a] Philip J. W. Moll,[a, b] Markus König,[a] Horst Borrmann,*[a] and Yuri Grin[a]

Abstract: In a joint effort utilizing modified sample preparation, microscopy, X-ray diffraction and micro-fabrication, it became possible to prepare single crystals of the "hidden" phase $AlCr_2$. High-resolution X-ray diffraction analysis is described in detail for two crystals with the similar overall composition, but different degree of disorder, which seems to be the main cause for the differing unit cell parameters. Chemical bonding analysis of $AlCr_2$ in comparison to prototypical $MoSi_2$ shows pronounced differences reflecting the interchange of main group element vs. transition metal as majority component.

Introduction

Among intermetallic compounds, the members of the $MoSi_2$ family are known mostly by the physical properties of the prototype – molybdenum disilicide. Having a moderate density, high melting point above 2000 °C and metallic conductivity, this compound is a base component of the materials for high-temperature heating elements.[1] In total, the Pearson Databank counts 41 representatives of the $MoSi_2$ structure type,[2] which may be further separated into groups based on their *c/a* ratio.[3] Representatives like $AlCr_2$ or $AlAu_2$[4] are, from the chemical point of view, difficult to ascribe to the $MoSi_2$ structure type at first glance. On the other hand, the chemically homologous phase $CrSi_2$ crystallizes in a closely related structure type, bearing its own name. At the same time, WSi_2[5] is found in $MoSi_2$-type, while WAl_2[6] displays $CrSi_2$ type structure. This analogy would indicate rather the opposite composition in the case of mentioned aluminides of chromium and gold, which lead even to consideration of $AlCr_2$ as an anti-$MoSi_2$ type.[7]

The aluminum-chromium system was heavily investigated for technological reasons, e.g. for use in high-temperature materials or Al-based alloys. In the course of investigations of the Al–Cr phase diagram,[8] $AlCr_2$ was commonly considered the Cr-richest binary compound, however, stable below about 900 °C only. Frequently called β-phase, it is not melting congruently, but forms by ordering of aluminum atoms on a slightly deformed body-centered cubic lattice upon cooling the solid solution of Al in Cr (α-phase). The homogeneity range of $AlCr_2$ is quite wide, extending from 65.5 to 71.2 at.% Cr, 78.6–82.8 wt.%, respectively.[9,10] In the present work, a modified synthesis route was applied to prepare and isolate single crystals of $AlCr_2$.

The crystal structure of $AlCr_2$ was first determined by Bradley and Lu in 1937.[11] It was described as a three-fold *bcc* supercell, where two layers of chromium atoms alternate with one layer of aluminum (Figure 1). The space group is *I*4/*mmm*, and with two formula units in the unit cell the structure is assigned to $MoSi_2$ type, $C11_b$.[12] While in $MoSi_2$ molybdenum and silicon atoms occupy Wyckoff positions 2*a* and 4*e*, respectively,[13] in $AlCr_2$ it is just the other way around, with the positions of transition metal and main group element interchanged. $MoSi_2$ may be considered as constructed from closest-packed pseudo-hexagonal layers consisting of Mo and Si atoms, stacked in AB sequence (with 2 + 2 rather than 3 atoms of the

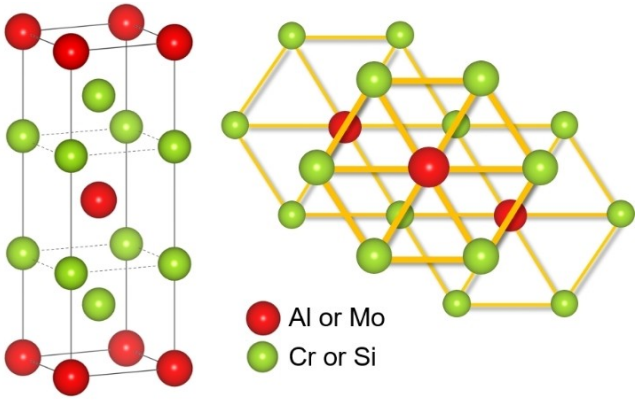

Figure 1. Left: unit cell of $AlCr_2$ (or $MoSi_2$), with basic bcc type cell indicated by broken lines. Right: stacking of pseudo-hexagonal layers along [110].

[a] M. D. Milosavljević, Dr. U. Burkhardt, Prof. Dr. P. J. W. Moll, Dr. M. König, Dr. H. Borrmann, Prof. Y. Grin
Max Planck Institute for Chemical Physics of Solids
Nöthnitzer Strasse 40, 01187 Dresden (Germany)
E-mail: Horst.Borrmann@cpfs.mpg.de

[b] Prof. Dr. P. J. W. Moll
École polytechnique fédérale de Lausanne
1015, Lausanne (Switzerland)

Supporting information for this article is available on the WWW under https://doi.org/10.1002/chem.202100817

next layer in contact with any atom in the previous layer) along the [110] direction of the body-centered tetragonal unit cell (Figure 1). This type of arrangement is regarded as derived from bcc packing.[14] However, instead of coordination number 8+6, the tetragonal distortion induces coordination numbers 10+4 for both components. Molybdenum atoms are surrounded by 10 silicon and 4 molybdenum atoms, while silicon atoms are surrounded by 5 Si and 5 Mo atoms, with 4 silicon atoms at larger distance.

The understanding of the structural analogy between chemically different $MoSi_2$ and $AlCr_2$ may be found via analysis of chemical bonding based on the precise crystal structure determination. The latter was largely hindered by the complex phase diagram of the Al–Cr system and inaccessibility of $AlCr_2$ from the liquid state causing lack of suitable single crystals for X-ray diffraction experiments.

Results and discussion

Preparation and microstructure analysis

As starting materials, Cr granules and Al foil were carefully weighed in an argon-filled glove box targeting the ideal composition and placed in an alumina crucible. Due to the difference in density between chromium and aluminum (7.19 vs. 2.70 g/cm^3), aluminum foil was placed at the bottom and sides of the crucible first and filled with chromium. In this way, chromium granules should pass through the liquid aluminum upon its melting. Granules of chromium rather than powder were used, due to lower oxygen content. The alumina crucible was placed in a quartz glass ampoule, evacuated down to 10^{-8} mbar and heated at a rate of 0.3 °C/min until the melting point of aluminum was reached and then slightly faster (0.6 °C/min) to 800 °C, under dynamic vacuum. Around the melting temperature of aluminum, pressure would temporarily rise to 10^{-6} mbar indicating release of a permanent gas passing a trap cooled with liquid argon. Annealing was done for 2 days, with slow cooling (0.6 °C/min) to ambient temperature afterwards. The sample was ground in a tungsten carbide mortar and pressed into a pellet for homogenization and the same annealing process was repeated. This time no permanent gas was released. For the following annealing steps, the ampoule was sealed under Ar atmosphere of around 800 mbar. The next step was to heat the sample to 1000 °C and anneal at this temperature for 2 h to enhance homogenization and diffusion, before lowering the temperature to 850 °C and continuing the annealing for 7 days.

This procedure was not enough to produce single-phase material, therefore, annealing was repeated until single-phase $AlCr_2$ was obtained. However, for any subsequent annealing step, the highest temperature was 850 °C. As a final thermal treatment, the sample was annealed at 800 °C for 500 h. Between these steps, progress was carefully monitored by powder diffraction (PXRD), and optical microscopy as well as scanning electron microscopy (SEM) based methods, for selected samples only.

Polarized light microscopy revealed strong orientation contrast of the $AlCr_2$ phase in contrast to the two cubic phases, Cr and solid solution α-Cr(Al) (Figures 2a, c), while differential interference contrast allowed identification of the pure Cr phase due to significant topography (Figure 3b). The comparison of these optical micrographs with the element distribution maps determined by energy dispersive X-ray spectroscopy (EDX) and material contrast images from back scattered electrons (BSE) in the SEM (Figure 3c), allowed spatially resolved assignment of the three phases. Particles where pure Cr is enveloped by α-Cr(Al) and $AlCr_2$ (Figure 3; Figure S1 Supporting Information) were observed in all samples, even in those where according to PXRD, only $AlCr_2$ phase was present. This phase arrangement reflects the diffusion dominated process of formation of the $AlCr_2$ phase, which is obviously the main reason why it is difficult to obtain homogenous single-phase material.

The evaluation of electron back scatter diffraction (EBSD) patterns resulted in the assignment of the two phases, α-Cr(Al) (here: $Al_{0.3}Cr_{0.7}$) and $AlCr_2$. However, there is no relation to grain or phase boundaries determined by above mentioned methods. Here, the quality of the experimental patterns allows the assignment to either one of the two phases, but it is not sufficient to distinguish between them by well-established pattern evaluation methods (Figures 2b,d). The assignment is additionally complicated by the similarity between the Kikuchi patterns, which comes from the close structural resemblance between these two phases.

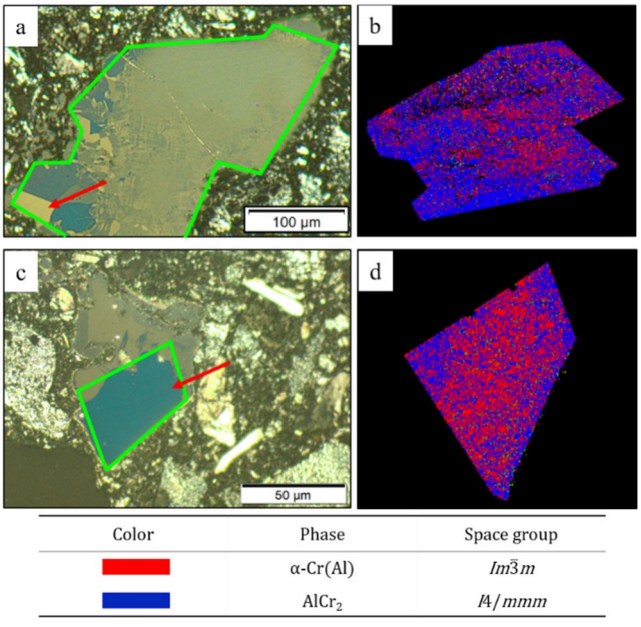

Figure 2. Multi-phase fragments of Al–Cr alloy used to extract $AlCr_2$ crystal 1 (top row) and crystal 2 (bottom) by FIB from marked grains (red arrows). Area enclosed in green is analyzed by EBSD. *Left column*: polarized light micrographs of $AlCr_2$ grains with strong orientation contrast next to α-Cr(Al) domains with homogeneous reflectivity. *Right column*: spatially resolved phase assignment of α-Cr(Al) and $AlCr_2$ according to EBSD pattern evaluation. All experimental patterns are assigned, but pattern quality is not sufficient to reliably distinguish between the two phases.

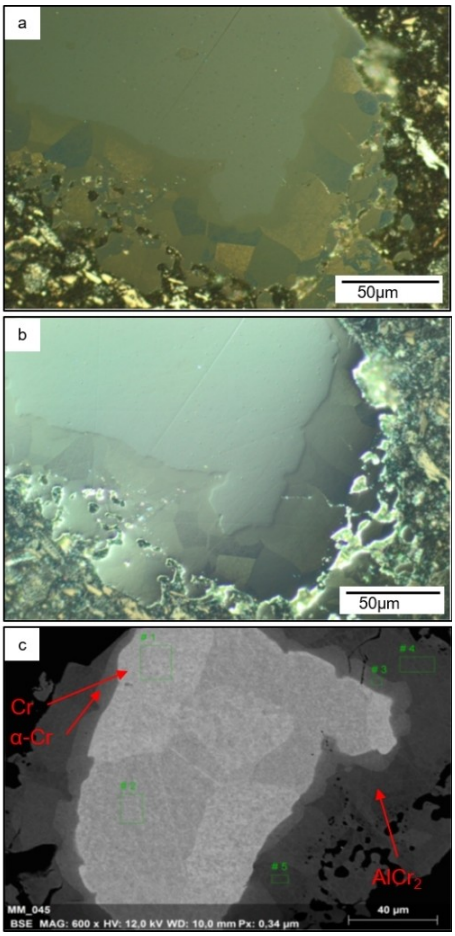

Figure 3. Micrographs with different contrast modes of Cr–Al fragment: a) polarized light contrast showing strong orientation contrast of the $AlCr_2$ phase; b) differential interference contrast (DIC) with strong topography of the Cr phase; c) material contrast using backscattered electrons (BSE), displaying Cr (white), α-Cr(Al) (bright grey) and $AlCr_2$ (dark grey) as indicated by the reduced electron yield in materials with smaller average atomic number.

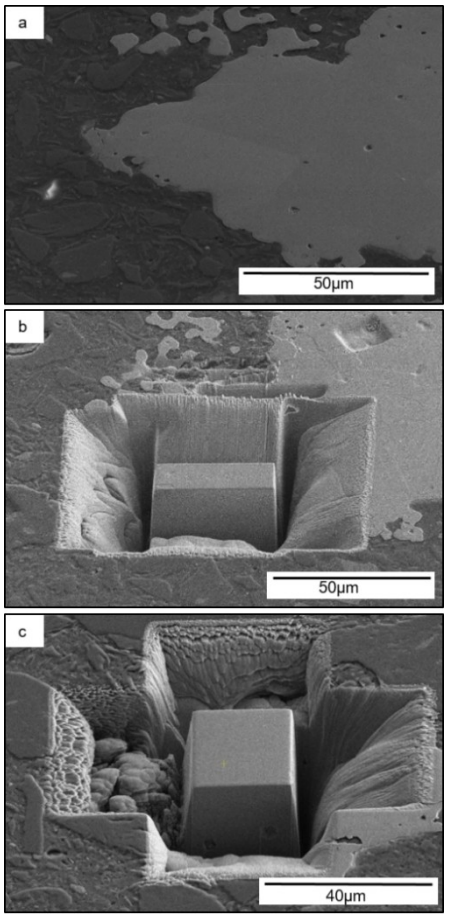

Figure 4. SEM images of $AlCr_2$ crystals obtained during FIB cutting, before lift-out. a) before and b) after cutting of crystal 1; c) crystal 2. Images were obtained with secondary electrons. Image c) shows two small holes in the cuboid, thus, final cutting was done slightly above them.

As anticipated from the phase diagram, growing single crystals of this material requires special efforts, since appropriate annealing temperatures are too low to achieve sizeable crystals within reasonable amount of time. A quite new approach applies micro-fabrication technology to isolate crystals for diffraction experiments from selected domains within a pressed polycrystalline entity.[15] Using a focused ion beam (FIB) technique, cuboid-like pieces were extracted from single grains that had been localized in the polycrystalline material on the basis of their uniform polarization contrast in the light microscope. This microfabrication approach allowed for the first detailed structure investigation of $AlCr_2$ single crystals. In the FIB procedure, the crystal is exposed by a Xenon ion beam from 4 sides (Figure 4) and an undercut except for a narrow bridge. Both crystals were finally extracted and mounted on a polyimide tip (MiTeGen MicroCrystal Mounts) with the help of a micromanipulator and a trace of grease (Apiezon H). Dimensions of the extracted grains were around $35\times15\times15$ µm^3 and $17\times16\times10$ µm^3 for crystal 1 and crystal 2, respectively (Figure 4).

The microstructure of respective samples is quite complex and only adequate combination of metallographic and diffraction methods allows identification and selection of suitable grains of $AlCr_2$ for further investigation. Furthermore, none of the above used analysis methods provides insight into the exact local distribution of atoms. For this kind of detailed structure analysis, investigations on single crystals are of paramount importance.

Single-crystal X-ray diffraction

The structural model for crystal 1 refined well in space group *I*4/*mmm*, with the overall completeness based on Laue symmetry of 99.4%, with 25 observations per parameter in refinement. Data collection information, together with quality indicators and crystallographic data are given in tables 1 and 2. The structure of $AlCr_2$ has only one adjustable positional parameter, *z* for the chromium atom. Its value in the present

Table 1. Single crystal data for $AlCr_2$.[16]

Parameter *Space group*	*Crystal 1* *I4/mmm*	*Crystal 2* *I4/mmm*
Composition	$AlCr_2$	$Al_{1.04}Cr_{1.96}$
a	3.0086(2) Å	3.0055(2) Å
c	8.6531(11) Å	8.6604(6) Å
V	78.325(13) Å^3	78.230(9) Å^3
μ [Mo-K_α]	13.76 mm^{-1}	13.81 mm^{-1}
N_{tot}	2231	1892
$N_{I>3\sigma(I)}$	1911	1737
N_{unique}	153	163
MoO	14.6	11.6
$2\theta_{min}$	6°	6°
$2\theta_{max}$	100°	104°
Measured range	$-6 \le h \le 6$ $-5 \le k \le 6$ $-18 \le l \le 18$	$-6 \le h \le 6$ $-4 \le k \le 4$ $-18 \le l \le 18$
R_{int}	4.09%	2.79%
R_σ	1.80%	1.53%
$R_{p.i.m.}$	0.74%	0.55%
mean $I/\sigma(I)$	15.4	17.0
Overall scale factor	14.38(4)	15.12(6)
Extinction *	none	0.117(9)
Refined param.	6	8
Refl. [$F_o > 4\sigma(F_o)$/all]	148/153	158/163
*R*1 [$F_o > 4\sigma(F_o)$/all]	2.02%/2.17%	1.38%/1.53%
*wR*2	4.03%	3.22%
GooF	1.120	1.147
Weighting coeff.*	0.0126/0.2052	0.0175/0.0102
Residual density:		
maximum	1.01 e Å^{-3} at (0 0 0.06) 0.52 Å from Al1	0.80 e Å^{-3} at (0.1 0.1 0) 0.52 Å from Al1 0.58 e Å^{-3} at (0 0 0.06) 0.49 Å from Al1
minimum	−1.54 e Å^{-3} at (0 0 0.41) 0.75 Å from Cr1	−0.81 e Å^{-3} at (0 0 0.46) 1.04 Å from Cr1

*as given in SHELXL manual [31b].

investigation agrees within 3 s.u.'s with the one determined by Bradley and Lu.[11]

In the peak list, obtained from difference Fourier synthesis, the maximum was located near the Al atom, while the minimum was near the Cr atom. In order to check for systematic errors, low-angle data ($\theta < 20°$) were omitted from the refinement. With this step, the number of unique reflections was reduced from 153 to 128. Quality indicators *R*1(all data) and *wR*2 increased slightly, as expected. The atomic displacement parameters increased very slightly, but the overall scale factor as well. Main features in Fourier difference map remained virtually unchanged. This confirms that the full data set does not contain any significant contributions originating from unaccounted absorption or extinction effects. Contributions originating from a non-spherical valence electron distribution around the atoms should have been minimized at this step, too. For better clarity, the difference electron density map was visualized for the whole data set in (110) plane, as shown in Figure 5a.

Bearing in mind that the $AlCr_2$ phase has a wide homogeneity range, along with its structure as the result after ordering aluminum atoms in a chromium structure, the possibility of chromium occupying the aluminum position and vice versa has to be considered. Moreover, it seems more likely both positions being mixed simultaneously, rather than only one of them. Accordingly, the occupancy of Al was refined with the occupancy of Cr fixed at 100% and vice versa (Table S2, Supporting Information). The change of the overall scale factor was largest in the case when Cr occupancy was refined, with site occupancy factor (s.o.f.) of Al fixed, while atomic displacement parameters (ADP) for Al increased in both cases, but those for chromium stayed the same. In both cases the final values showed insignificant deviation from 100% occupancy.

Obviously, data for this particular crystal provide no indication towards deviation from ideal 1:2 composition, nor towards significant anti-site occupancies. As an additional test, the form factor on the chromium site was changed to its lighter neighbor, vanadium, whose occupancy was also refined. The resulting value was above full occupancy (Table S4, Supporting Information), well in agreement with the previous conclusion.

The structural model for crystal 2 refined in space group *I*4/*mmm*, with the overall completeness based on Laue symmetry of 98.8% and 2 unique reflections missing (Table 1).

Maxima in the Fourier peak list were located near aluminum site but a minimum near Cr position, like in the case of crystal 1.

As opposed to crystal 1, omitting of the low-angle data below $\theta = 20°$ changed only moderately the value of the second residual peak in the vicinity of the aluminum atom, while the first one disappeared. The difference electron density in the (110) plane, for the whole data set, is depicted in Figure 5b.

For the investigation of mixed occupancy, following procedure was applied: the occupancies of either aluminum or chromium atom were refined in the same manner as for crystal 1. The values were calculated to 103.0(5) and 97.1(5)% for Al and Cr site, respectively. In contrast to crystal 1, the

Table 2. Positional and atomic displacement parameters (Å^2) for final models of crystals 1 and 2 of $AlCr_2$.

	Atom	Site	*x*	*y*	*z*	Occupancy †	$U^{11} = U^{22}$	U^{33}*	U_{eq}
Crystal 1	Al1	2*a*	0	0	0	1	0.0053(2)	0.0067(3)	0.0058(2)
	Cr1	4*e*	0	0	0.32010(4)	1	0.00554(9)	0.0064(1)	0.00583(7)
Crystal 2	Al1	2*a*	0	0	0	0.96	0.0060(1)‡	0.0070(2)	0.0063(1)
	Cr2					0.04			
	Cr1	4*e*	0	0	0.32004(2)	0.96	0.00500(8)	0.00526(9)	0.00508(7)
	Al2		0	0	0.345(2)	0.04			

*$U^{23} = U^{13} = U^{12} = 0$ for both sites. U_{eq} is defined as 1/3 of the trace of the orthogonalized U_{ij} tensor. ‡ Displacement parameters in case of crystal 2 are constrained. † Occupancies in case of crystal 2 are fixed for both Al1 and Cr1 (details in text).

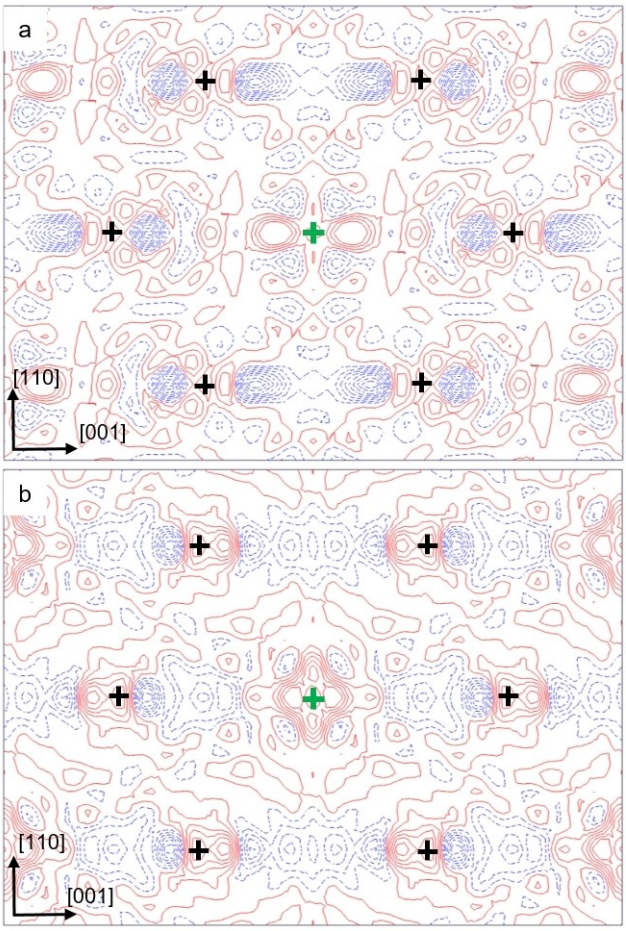

Figure 5. Residual density in (110) plane for crystal 1 (a) and crystal 2 (b). Red contours represent positive values and blue negative ones (increment 0.2 e Å^{-3}). Positions of atoms are labeled with crosses, green for aluminum and black for chromium.

numbers give strong indication of anti-site occupancy of at least 3%. Furthermore, aluminum and chromium positions were refined individually as mixed by adding Cr2 on the Al1 site or Al2 on the Cr1 site. In any case, the total occupancy of the refined site was constrained to unity and ADP's of both atoms were kept equal. When Cr1 site was refined as mixed, the *z* parameter of either atom was not constrained. In both cases, the reliability factors decreased as well as the residual electron density. The occupancy was calculated to around 96:4% and 92:8% in case of Al1/Cr2 or Cr1/Al2 site, respectively. Finally, both sites were refined as mixed with the following procedure. First Al1 site was refined as mixed and the obtained s.o.f. values were fixed. Only then was the occupancy of Cr1 site refined. The reverse procedure was also done, starting with the refinement of Cr1 site. The result of the final refinement depended on the choice of the first site to be refined as mixed. In the former case, as the occupancy of Al1 was fixed at 96%, the refinement of Cr1 occupancy resulted in 96.6(9)%. Conversely, when Cr1 occupancy was fixed at 92%, the refinement of Al1 occupancy resulted in the value of 99.4(7)%. In the latter case, the positional parameter *z* of Cr1/Al2, had strong correlation with ADP's and overall scale factor, which in turn influenced the electron density at the Al1 position. The values of site occupancies in any case did not change significantly with omitting of low-angle data. Based on all data, it was concluded that the amount of the second element on either position has to be around 4% for this particular crystal. Therefore, occupancies of Cr2 and Al2 were fixed at this value, which means that the overall composition corresponds to an Al-rich one. The fit of the model was significantly improved with introduction of 4% of mixed occupancy on both sites (Table S1, Supporting Information). With respect to the value of positional parameter *z* at Cr1 site when full occupancy is assumed, the majority element, Cr1, moves closer to Al1 along the *c*-axis. The minority component, Al2, moves in opposite direction (Table S3, Supporting Information). Taking as reference the ideally ordered structure of $AlCr_2$, in which interatomic distances along *c*-axis are alternating as short between Al–Cr and long between Cr–Cr atoms, it is clear that the result is reasonable. This may be interpreted as a Peierls-type distortion in consequence of the ordering with respect to the arrangement in the α-phase.

Comparison of lattice parameters of isolated crystals of $AlCr_2$ shows small, but significant difference between crystal 1 and crystal 2, with the values of the former being closer to those given in [8] for the ideal composition (cf. Table 1). In previous investigations of the $AlCr_2$ phase, it was concluded that with higher chromium content in the structure, the unit cell parameter *a* decreases, but *c/a* ratio increases towards the ideal value of 3.[3,10] However, present results suggest that disorder, via anti-site occupancies, needs to be considered as another origin for changes in lattice parameters. Obviously, such insight is only accessible through single crystal investigations as these effects are likely levelled out in powder samples.

The calculated electronic density of states for the ordered model (crystal 1) of $AlCr_2$ (Figure 6) contains three well separated regions. The first one ($E < -2$ eV) is built mainly of the s and p states of Al and Cr with dominating contributions of Cr-d mainly between -4 eV and -2 eV. The second one (-2 eV $< E < -0.6$ eV) is built mainly by Cr-d states with contributions of Al-p and Cr-p states. A pseudo-gap separates this region from the third one (-0.6 eV $< E < E_F$). The latter is

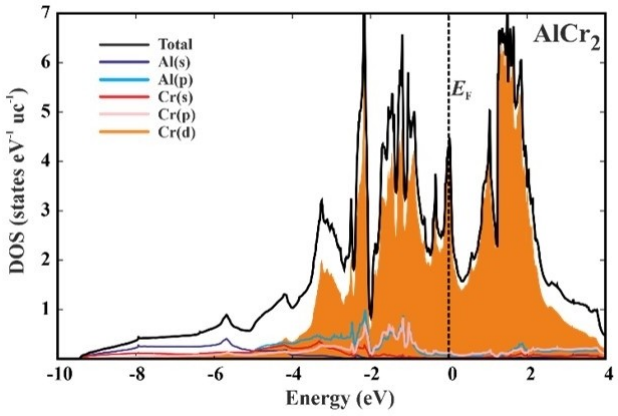

Figure 6. Electronic density of states for $AlCr_2$ with the atomic contributions.

formed practically by Cr-d with minor admixture of Al-p and Cr-p states. A special feature of this range is the location of the Fermi level at a peak of DOS, suggesting a general instability of the structural pattern. This is in agreement with the formation of $AlCr_2$ by a solid state reaction from the solid solution α-Cr(Al) and its further structural transformation at lower temperatures.[17] On the other hand, the same region defines the metallic behavior of $AlCr_2$.

The question about the bonding mechanism for the stabilization of the $MoSi_2$-type structural pattern in $AlCr_2$ and in the prototype $MoSi_2$ was studied by the electron localizability approach (ELI–D).[18]

First, the effective charges of atomic species were evaluated from the calculated electron density. The zero-flux surfaces in the gradient vector field of electron density form the boundaries of electron density basins, which represent atomic regions within the framework of Quantum Theory of Atoms in Molecules (QTAIM[19]). Then the electron density was integrated in spatial regions, defined in QTAIM. Their electronic populations yield the QTAIM effective atomic charges. The obtained charge transfer of 0.27 e^- per Cr atom (Figure 7, top) is rather large in comparison with the small difference in electronegativity between the components as per the Allred-Rochow scale (1.5 for Al and 1.6 for Cr) and even is not in agreement with the electronegativity difference between Al and Cr according to Sanderson (1.54 for Al and 1.35 for Cr) or Pauling (1.6 for Al, 1.56 for Cr) scales, but indicates substantial ionic contribution to the bonding in this compound. Despite clearly larger electronegativity of silicon in comparison with molybdenum according to all three scales mentioned above, the effective charges are much smaller: +0.18 for Mo and −0.09 for Si, respectively (Figure 7, bottom).

The analysis of the electron localizability indicator delivered further details of the atomic interactions in $AlCr_2$ and $MoSi_2$. The distribution of ELI–D in $AlCr_2$ is characterized by structuring of the penultimate shell of Cr indicating the participation of the (d)-electrons in the bonding and by appearance of three types of attractors (maxima) in the valence region (Figure 7, top). The first one is located on the line between the aluminum atoms in the octahedral hole (green octahedron in Figure 7 top). Its basin contains 1.16 electrons contributed by two Al and 4 Cr atoms, i.e. it visualizes a six-atomic bond. Two others are located in the tetrahedra formed either by one Al and three Cr atoms (marked red in Figure 7, top) or by four Cr atoms (marked blue in Figure 7 top), i.e. they reveal four-atomic interactions. The total number of 15.52 electrons per unit cell in the valence region reveals the contribution of 0.76 (d-)electrons from the penultimate shell per Cr atom in the bonding events within the valence region. Appearance of multi-atomic interaction may be expected for $AlCr_2$ considering the valence electron count (VEC) of 7/3 which is much lower in comparison with the 4 e^- per atom in the anionic part required to realize a Zintl-like mechanism as in CaC_2.

In case of $MoSi_2$, the maxima of ELI–D are located on the short Mo–Si contacts along [001] (cyan in Figure 7, bottom) or close to Mo–Si contacts connecting the neighboring atomic nets (pink in Figure 7, bottom). Former visualize the two-atomic bonds (bond basin population 1.37 e^-), the latter – three-atomic bonds (0.99 e^- per bond). The total number of 21.48 electrons in the valence region reveals the contribution of 0.74 (d-) electrons from the penultimate shell per Mo atom in the

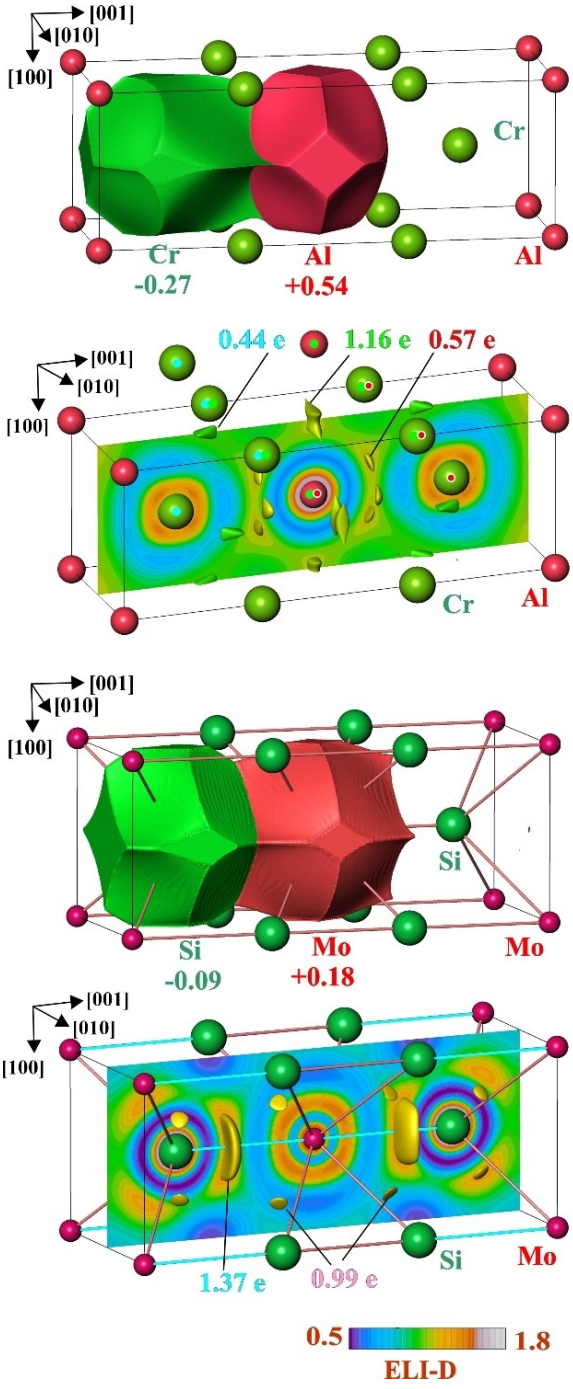

Figure 7. Chemical bonding in $AlCr_2$ (top) and $MoSi_2$ (bottom) from the electron-localizability approach: upper panels show shapes of the QTAIM atoms and their effective charges; lower panels show distributions of the electron-localizability indicator in the (020) plane with the iso-surfaces visualizing the location of the ELI–D maxima: for $AlCr_2$ – in the octahedral (green marked contributing atoms) and tetrahedral (red and cyan marked contributing atoms) holes; for $MoSi_2$ – on or close to the short Mo–Si contacts (cyan and pink).

bonding events within the valence region. Reduction of the number of atoms participating in each bonding event and appearance of the two-atomic bonds can be understood considering larger VEC of 10/3 in $MoSi_2$. Interesting is the fact, that the total number of 10 electrons per formula unit would allow also a Zintl-like bonding description, like in $Ca^{2+}[(3b)C^{1-}]_2$, which is assigned the same Pearson symbol, but differs from the $MoSi_2$ type by much smaller *c/a* ratio, along with markedly larger value of the *z* coordinate for the carbon atom at the 4*e* site.

Overall, this family of isopointal structures represents a very large flexibility, which is also reflected in four different branches assigned to this structure type, namely CaC_2-, $MoSi_2$-, Zr_2Cu-[20] and XeF_2[21] branch. Both terminal members, CaC_2- and XeF_2 type,[22,23b] respectively, exhibit very similar *c/a* ratio, but a decisive difference among the *z*-parameters of the majority component. The latter directly reflects the change of characteristic structural units from C_2 dumbbells to linear XeF_2 molecules. All intermetallic relatives do not contain such distinct units, nevertheless, the $MoSi_2$ branch reflects more closely the CaC_2 type, while the Zr_2Cu branch leans more towards XeF_2. Within the intermetallic branches, the *c/a* ratio changes in a quite wide range, while *z*-parameter remains close to 1/3. However, only very few intermetallic structures belonging to the $MoSi_2$ and Zr_2Cu branch have been studied in detail from single crystal data, which is something to be taken into account before discussing fine structural and bonding features. Even more important is the experimentally observed "polymorphism" in these structures with very small additions of a third element.[24] Nevertheless, taking only the *c/a* ratio into consideration, $AlCr_2$ nicely reflects the transition from $MoSi_2$ to Zr_2Cu branch, where some authors assigned it even to an additional type.[12]

The rather large charge transfer from Al to Cr and localization of the ELI–D maxima in the octahedral holes of the formally *bcc* atomic pattern of $AlCr_2$ reveals its close bonding relationship to the elements, where the ELI–D maxima usually appear within the octahedral or tetrahedral holes.[25] On the other hand, the ELI–D distribution in the prototype $MoSi_2$ reveals maxima on the Mo–Si contacts and unusually low charge transfer. Summarizing, despite the formal crystallographic assignment to the same family of structures and even same structure type, both compounds investigated in this study reveal clearly different bonding patterns, justifying – at least partially – the assignment of a separate branch for $AlCr_2$.[3] Furthermore, these findings support one of the more general features of intermetallic compounds–stabilization of isopointal atomic arrangements by different bonding patterns.

Experimental section

In the present study, $AlCr_2$ single crystals have been prepared starting from the elements, Cr (ChemPUR, 99.98%) and Al (Alfa Aesar, 99.999%), weighed for a stoichiometric ratio up to a total weight of around 0.5 g. For EDX and EBSD analyses, all samples were examined with electron microscope JEOL JSM-7800F Schottky field emission scanning electron microscope, equipped with dual EDX/EBSD analysis system from Bruker, QUANTAX CrystAlign400, with e-Flash EBSD detector including the ARGUS backscattered/forescattered electron imaging system. Acceleration voltage of 15 kV was used. In preparation for EDX/EBSD analysis samples were grinded with silicone carbide (SIC) grinding paper and subsequently polished using diamond abrasive down to 0.25 μm particle size. For extraction of single crystals of $AlCr_2$ from the polycrystalline sample by FIB, a FEI-Helios PFIB instrument, with xenon plasma beam was used at beam voltage of 30 kV. Initial coarse cuts were performed using a high ion current of 2.5 μA, followed by subsequent lower current milling at 60 nA to improve the cuboid-like shape of the specimen.

Single crystal X-ray diffraction data for crystal 1 and crystal 2 were collected at ambient temperature (295 K) up to high resolution ($\sin\theta/\lambda = 1.08$ and 1.11, respectively) on a 4-circle diffractometer, Rigaku AFC7, equipped with graphite monochromator (Mo-K_α radiation, $\lambda = 0.71073$ Å) and Saturn724+ CCD detector, in 2×2 binning mode. Data collection and reduction were done with the program CrystalClear,[26] including integration with d*TREK software[27] and multi-scan absorption correction based on Blessing's algorithm.[28] For both crystals several φ-scans were recorded. For crystal 1, low- and high-angle scans were collected with 0.6° image width and exposure time of 45 and 70 seconds, respectively. In case of crystal 2, the low angle scan was recorded with an image width of 0.6° and 50 s exposure time, while high-angle scans were done in steps of 0.5° and 80 s. Separate scans were scaled and merged together with the help of SORTAV[29] as included in the program package WinGX (version 2014.1).[30] The refinement was done by full-matrix least squares methods on F^2, as implemented in SHELXL.[31]

For better assessment of the residual density during the refinement process, difference electron density maps in a specified plane were used. Command "LIST 3" was added to input data in SHELXL, which created an *fcf*-file with observed and calculated structure factors. This file was then used for calculation of difference Fourier synthesis and visualization of the maps (Figure 5) with the help of the program VESTA.[32]

The electronic structure calculation and bonding analysis for $AlCr_2$ were performed using experimental values of lattice parameters and atomic coordinates (Tables 1 and 2) using the all electron, local orbital full–potential method (FPLO) within the local density approximation (DFT/LDA).[33] The Perdew-Wang para-metrization was employed.[34]

The analysis of the chemical bonding in $AlCr_2$ was performed by means of the electron localizability approach in position space.[18] Electron localizability indicator (ELI) in its ELI–D representation[35,36] together with the electron density (ED) was calculated with a specialized module implemented within FPLO code.[37] The topology of ELI–D and ED was evaluated with the program DGrid.[38] To obtain the atomic charges from ED and bond populations for bonding basins from ELI–D were obtained by the integration ED and ELI–D within the basins (space regions), bounded by zero-flux surfaces in the according gradient field. This procedure follows the quantum theory of atoms in molecules (QTAIM[19]). Combined analysis of ED and ELI–D yields basic information for the description of the bonding situation in solids,[39–41] in particular for the intermetallic compounds.[42–44]

Acknowledgements

The authors acknowledge Dr. F. R. Wagner for fruitful discussions. Open Access funding enabled and organized by Projekt DEAL.

Conflict of Interest

The authors declare no conflict of interest.

Keywords: crystal structure · disorder · focused-ion beam · intermetallic phase · single crystal growth

[1] Kanthal, Swedish Patent **1953**, *155*, 836.
[2] P. Villars, K. Cenzual, Pearson's Crystal Data: Crystal Structure Database for Inorganic Compounds (on DVD), Release 2018/19, ASM International, Materials Park, Ohio, USA.
[3] A. Raman, K. Schubert, *Z. Metallkd.* **1964**, *55*, 704–710.
[4] M. Pušelj, K. Schubert, *J. Less-Common Met.* **1974**, *35*, 259–266.
[5] A. N. Christensen, *J. Cryst. Growth* **1993**, *129*, 266–268.
[6] Q. F. Gu, D. Y. Jung, G. Krauss, W. Steurer, *J. Solid State Chem.* **2008**, *181*, 2719–2724.
[7] E. Parthé, L. Gelato, B. Chabot, M. Penzo, K. Cenzual, R. Gladyshevskii, *TYPIX. Standardized Data and Crystal Chemical Characterization of Inorganic Structure Types. Gmelin Handbook of Inorganic and Organometallic Chemistry, Vol. 4*, Springer, Berlin, **1993/1994**, p. 1278.
[8] M. Ellner, J. Braun, B. Predel, *Z. Metallkd.* **1989**, *80*, 374–383.
[9] A. J. Bradley, S. S. Lu, *J. Inst. Met.* **1937**, *60*, 319–337.
[10] W. Köster, E. Wachtel, K. Grube, *Z. Metallkd.* **1963**, *54*, 393–401.
[11] A. J. Bradley, S. S. Lu, *Z. Kristallogr.* **1937**, *96*, 20–37.
[12] Around that time, Ewald and Hermann were collecting and compiling data of available crystal structures in the *Strukturbericht* journal, where compounds were assigned a structure type designation according to different rules, such as number of constituting elements and type of the lattice. Designation C48 was assigned to $AlCr_2$, where C represents a binary compound with AX_2 formula, while the number was assigned historically, as new compounds were reported.[45] However, almost twenty years later this designation was not used anymore, instead $AlCr_2$ is described as geometrically isotypic to $MoSi_2$, which itself is assigned $C11_b$ designation.[46] In the following years, few articles were dealing with the division of the $C11_b$ structure type into several branches, of which one belongs to the $AlCr_2$ structure.[3,23] The criteria used were *c/a* ratio or/and coordination environment. However, in many of the articles dealing with investigations of $AlCr_2$ which were done after 1965, this structure was presented simply as a member of $MoSi_2$-structure type family.
[13] W. H. Zachariasen, *Z. Phys. Chem. Stoechiom. Verwandtschaftsl.* **1927**, *128*, 39–48.
[14] W. B. Pearson, *The Crystal Chemistry and Physics of Metals and Alloys*, Wiley, New York, **1972**, p. 588.
[15] V. Sunko, P. H. McGuinness, C. S. Chang, E. Zhakina, S. Khim, C. E. Dreyer, M. Konczykowski, H. Borrmann, P. J. W. Moll, M. König, D. A. Muller, A. P. Mackenzie, *Phys. Rev. X* **2020**,*10*, 021018_1–16.
[16] Deposition Numbers 2067301, and 2067302 contain the supplementary crystallographic data for this paper. These data are provided free of charge by the joint Cambridge Crystallographic Data Centre and Fachinformationszentrum Karlsruhe Access Structures service www.ccdc.cam.ac.uk/structures.
[17] *Binary Alloy Phase Diagrams, Vol. 1, 2nd ed.* (Ed. T. B. Massalski), ASM International, Materials Park, **1990**, p. 138.
[18] F. R. Wagner, V. Bezugly, M. Kohout, Yu. Grin, *Chem. Eur. J.* **2007**, *13*, 5724–5741.
[19] R. F. W. Bader, *Atoms in molecules: A quantum theory*, Oxford University Press, Oxford **1999**.
[20] M. V. Nevitt, J. W. Downey, *Trans. Metall. Soc. AIME* **1962**, *224*, 195–196.
[21] H. A. Levy, P. H. Argon, *J. Am. Chem. Soc.* **1963**, *85*, 241–242.
[22] E. Parthé, *Elements of Inorganic Structural Chemistry. Selected efforts to predict Structural Features*, 2nd Ed., Petit-Lancy: K. Sutter Parthé, **1996**.
[23] a) E. Hellner, W. B. Pearson, *Z. Kristallogr.* **1984**, *168*, 273–291; b) P. Paufler, G. Just, *Z. Kristallogr.* **1996**, *211*, 777–793.
[24] M. D. Milosavljević, U. Burkhardt, A. Leithe-Jasper, Yu. Grin, H. Borrmann, **2021**, submitted.
[25] Yu. Grin, A. Savin, B. Silvi in *The Chemical Bond: Chemical Bonding Across the Periodic Table, Vol. 1*, Wiley-VCH, Weinheim, **2014**, p. 345.
[26] Rigaku. *CrystalClear-SM Expert 2.0 r2*. **2009**.
[27] J. W. Pflugrath, *Acta Crystallogr.* **1999**, *D55*, 1718–1725.
[28] R. H. Blessing, *Acta Crystallogr.* **1995**, *A51*, 33–38.
[29] R. H. Blessing, *Crystallogr. Rev.* **1987**, *1*, 3–58.
[30] L. J. Farrugia, *J. Appl. Crystallogr.* **2012**, *45*, 849–854.
[31] a) G. M. Sheldrick, *Acta Crystallogr.* **2015**, *C71*, 3–8; b) https://shelx.uni-goettingen.de.
[32] K. Momma, F. Izumi, *J. Appl. Crystallogr.* **2011**, *44*, 1272–1276.
[33] K. Koepernik, H. Eschrig, *Phys. Rev. B* **1999**, *59*, 1743–1757.
[34] J. P. Perdew, Y. Wang, *Phys. Rev. B* **1992**, *45*, 13244–13249.
[35] M. Kohout, *Int. J. Quantum Chem.* **2004**, *97*, 651–658.
[36] M. Kohout, *Faraday Discuss.* **2007**, *135*, 43–54.
[37] A. Ormeci, H. Rosner, F. R. Wagner, M. Kohout, Yu. Grin, *J. Phys. Chem. A* **2006**, *135*, 1100–1105.
[38] M. Kohout, DGrid, versions 4.6-5.0, **2018**.
[39] M. Kohout, A. Savin, *Int. J. Quantum Chem.* **1996**, *60*, 875–882.
[40] Yu. Grin in: *Comprehensive Inorganic Chemistry II, Vol 2*, Elsevier, Oxford, **2013**, p. 359.
[41] Yu. Grin, A. Savin, B. Silvi, *The Chemical Bond: Chemical Bonding Across the Periodic Table*, Wiley-VCH, Weinheim, **2014**, p. 345.
[42] D. Bende, F. R. Wagner, Yu. Grin, *Inorg. Chem.* **2015**, *54*, 3970–3978.
[43] F. R. Wagner, R. Cardoso-Gil, B. Boucher, M. Wagner-Reetz, J. Sichelschmidt, P. Gille, M. Baenitz, Yu. Grin, *Inorg. Chem.* **2018**, *57*, 12908–12919.
[44] R. Freccero, P. Solokha, S. De Negri, A. Saccone, Yu. Grin, F. R. Wagner, *Chem. Eur. J.* **2019**, *25*, 6600–6612.
[45] P. P. Ewald, C. Hermann, *Strukturbericht 1937*, *Ergänzungsband 5*, **1940**, p. 5 and p. 53.
[46] K. Schubert, *Z. Naturforsch.* **1957**, *12a*, 310–319.

Manuscript received: March 5, 2021
Accepted manuscript online: April 30, 2021
Version of record online: July 12, 2021

